Article

Decadal Scale Changes in Glacier Area in the Hohe Tauern National Park (Austria) Determined by Object-Based Image Analysis

Benjamin Aubrey Robson [1],*, Daniel Hölbling [2], Christopher Nuth [3], Tazio Strozzi [4] and Svein Olaf Dahl [1]

[1]   Department of Geography, University of Bergen, Fosswinckelsgate 6, Bergen 5007, Norway; svein.dahl@uib.no
[2]   Department of Geoinfomatics-Z_GIS, University of Salzburg, Schillerstrasse 30, Salzburg 5020, Austria; daniel.hoelbling@sbg.ac.at
[3]   Department of Geosciences, University of Oslo, Postboks 1047 Blindern, Oslo 0316, Norway; christopher.nuth@geo.uio.no
[4]   GAMMA Remote Sensing, Worbstr. 225, Gümligen 3073, Switzerland; strozzi@gamma-rs.ch
*   Correspondence: benjamin.robson@uib.no; Tel.: +47-5558-3077

Abstract: In this paper, we semi-automatically classify clean and debris-covered ice for 145 glaciers within Hohe Tauern National Park in the Austrian Alps for the years 1985, 2003, and 2013. We also map the end-summer transient snowline (TSL), which approximates the annual Equilibrium Line Altitude (ELA). By comparing our results with the Austrian Glacier Inventories from 1969 and 1998, we calculate a mean reduction in glacier area of 33% between 1969 and 2013. The total ice area reduced at a mean rate of 1.4 km^2 per year. This TSL rose by 92 m between 1985 and 2013 to an altitude of 3005 m. Despite some limitations, such as some seasonal snow being present at higher elevations, as well as uncertainties related to the range of years that the LiDAR DEM was collected, our results show that the glaciers within Hohe Tauern National Park conform to the heavy shrinkage experienced in other areas of the European Alps. Moreover, we believe that Object-Based Image Analysis (OBIA) is a promising methodology for future glacier mapping.

Keywords: glacier mapping; OBIA; landsat; change detection; Alps; snowline; classification

1. Introduction

Glacier change is among the best natural indicators of climate change [1]. The European Alps have undergone a sharp decline in glacier area in recent decades [2–4] which can impact runoff [5], hydro-electric power production [6], hazards such as rockfalls and debris flows [7], and tourism [8]. Due to the time-consuming nature of carrying out *in situ* glacier measurements, many recent studies have opted for remotely sensed data to assess changes in glacier area [9], volume [10], and velocity [11] over various portions of the European Alps. Remote sensing data, such as satellite images, allow glacier area changes to be quantified at the regional scale, often using semi-automated methods. The strong spectral signature of clean ice makes it easy to identify in the Near-Infrared (NIR) and Shortwave-Infrared (SWIR) portions of the electromagnetic spectrum [12]. Band ratios and spectral indices that use the NIR and SWIR spectral bands, such as the Normalized Difference Snow Index (NDSI), are therefore well suited for semi-automatic mapping of clean ice, and have been used extensively in the European Alps [4,13,14]. Clean ice reflects 25%–35% less visible radiation than fresh snow, thereby allowing the end-of-season snowline or transient snowline (TSL) to be mapped [15].

The TSL can be used as an approximation of the equilibrium line altitude (ELA), the altitude on the glacier where the rate of accumulation equals the rate of ablation. The ELA is often used as a proxy for glacier mass balance, so by mapping the TSL on a regional scale, information about the health of the glaciers can be extracted [16]. The Global Land Ice Measurements from Space (GLIMS) initiative aims to provide a framework for assessing glacier changes using remotely sensed data, and to construct a global glacier inventory containing, among other information, data about the glacier size, the elevation of the TSL and the presence of supraglacial debris.

Debris-covered ice (rockfall and avalanche material overlaying the glacier ice) remains a problem in automated glacier mappings. The spectral similarity of supraglacial debris to the surrounding terrain inhibits mapping debris-covered ice automatically by using only spectral information. Auxiliary data such as thermal [17], morphological, [18] or coherence images between two Synthetic Aperture Radar (SAR) images (henceforth referred to as SAR coherence data) [19,20] must therefore be used in classifications. The mapping of debris-covered ice mostly requires manual mapping or correction and, as such, takes up a significant amount of time and effort in glacier mapping. Object-Based Image Analysis (OBIA) is a relatively new and emerging methodology within Geographic Information Systems Science or GIScience [21]. By working at the object level instead of the pixel level (PBIA or Pixel-Based Image Analysis), additional information such as spatial, contextual, hierarchical or textural information can be used to assign objects to classes. OBIA also permits the handling of multiple datasets (for example optical, topographic, SAR, vector) for classifying objects.

Little work to date has been done using OBIA to map glaciers. Rastner *et al.* [22] obtained very high (94.5% and 98.6%) accuracies working in the clean ice regions of the Canadian Coast Mountains and Greenland, respectively. The authors concluded that OBIA offered more advantages for applications on debris-covered glaciers than on clean ice. The studies that have used OBIA for glacier mapping have often focused on the delineation of debris-covered glaciers. Rastner *et al.* [22] obtained an accuracy of 88.5% in the Everest Region of Nepal. Robson *et al.* [20] used SAR coherence data in combination with optical and topographic data to map glaciers in the Manaslu Region of Nepal to an accuracy of 91%. The International Centre for Integrated Mountain Development (ICIMOD) used OBIA to assess decadal changes in Nepal [23] and Bhutan [24], as well as to map glaciers over the entire Himalayas [25]. The only time OBIA has been used in the European Alps was by Eisank *et al.* [26], who solely used the surface curvature to delineate cirque glaciers. To date, no work has been conducted performing multi-temporal OBIA classifications to assess glacier change over time.

Two glacier inventories have been conducted in Austria, both based on aerial photography from 1969 (henceforth referred to as AGI_1969) and 1996–2002 (with most images acquired in 1997 and 1998, henceforth referred to as AGI_1998) [27]. A 17% decrease in glacier area occurred between the two inventories [9]. LiDAR campaigns over the Austrian Alps were conducted between 2006 and 2013 by the regional governments [28–30]. The LiDAR dataset covers a range of years that has been collated together. This is clearly a source of error and is discussed in Section 5.3.

Several authors have calculated glacier area changes by using the Austrian Glacier Inventories, LiDAR data, or additional data. A change in glacier area of 8.2% was found for glaciers in the Ötztal Alps between the LiDAR data (acquired in this case in 2006) and AGI_1998 [31] while Schicker [32] used Landsat Thematic Mapper (TM) data to find an accelerating shrinkage of glaciers (13.3% between 1969 and 1985 and 21.8% between 1997 and 2003) for the Stubai Alps. Paul *et al.* [4] used 10 Landsat TM scenes to map glacier ice over the entire European Alps which was then submitted to GLIMS. Due to inconsistencies such as the interpretation of snow patches, no change assessment with the two previous Austrian Glacier Inventories could be conducted; however, a difference of 30% or 2% per year was found when the 2003 data were compared to the World Glacier Inventory (WGI) data from 1970 ± 15 years.

In this paper, we combine Landsat 5 and Landsat 8 imagery with a LiDAR-based DEM to map glacier outlines and transient snowlines in the Hohe Tauern National Park, Austria, for the years 1985, 2003, and 2013 and assess the change. The Austrian Glacier Inventories from 1969 and 1998 were

also used for comparison. We evaluate the potential of using high-resolution topographic data within OBIA to semi-automatically delineate debris-covered ice based on breaks in the surface morphology. Lastly, we create manually corrected glacier outlines with reference to the LiDAR DEM, SAR coherence data, and the change in surface elevation between the LiDAR DEM and the SRTM (Shuttle Radar Topography Mission). The SRTM DEM is a near-global (56° S to 60° N) elevation model acquired using the Space Shuttle Endeavour in February 2000 [33]. The SRTM1 product can be downloaded for free from the USGS Earth Explorer (earthexplorer.usgs.gov) and offers a spatial resolution of 1 arc-second (approximately 30 m).

The objectives of this paper are two-fold:

(1) To semi-automatically assess the changes in glacier area in Hohe Tauern National Park in the Austrian Alps by using Object-Based Image Analysis (OBIA).

(2) To assess the potential of using high resolution topographic data to detect debris-covered ice by using edge detection of the surface slope. Although debris-covered ice is not of a major concern in the Austrian Alps, other glacierized regions such as the Himalayas contain considerable amounts of debris-covered ice and, as such, any semi-automatic methods would be beneficial for estimating ice reserves and assessing glacier change.

2. Study Area and Data Used

Hohe Tauern National Park (HTNP) covers approximately 1800 km^2 between the federal states of Carinthia, Salzburg and Tyrol in western Austria (Figure 1). Approximately 10% (125 km^2) of HTNP is covered by glaciers [3], ranging in altitude from 2000 to 3600 m with the majority of glaciers situated between 2700 and 3100 m. The glaciers present are a mixture of clean ice and debris-covered glaciers. HTNP includes the Pasterze Glacier (17.6 km^2) (Figure 2), the largest glacier in the Austrian Alps; 1.2 km^2 of the Pasterzr Glacier is covered by supraglacial debris which reaches 47 cm in thickness towards the glacier terminus [34]. The majority of Austrian glaciers are less than 1 km^2 and only five glaciers in the country are larger than 10 km^2 [27]. Glaciers in the Austrian Alps can exist above ~2080 m, and sometimes at lower elevations due to higher-than-average accumulation primarily because of leeward accumulation caused by wind, or due to supraglacial debris insulating the underlying ice [8].
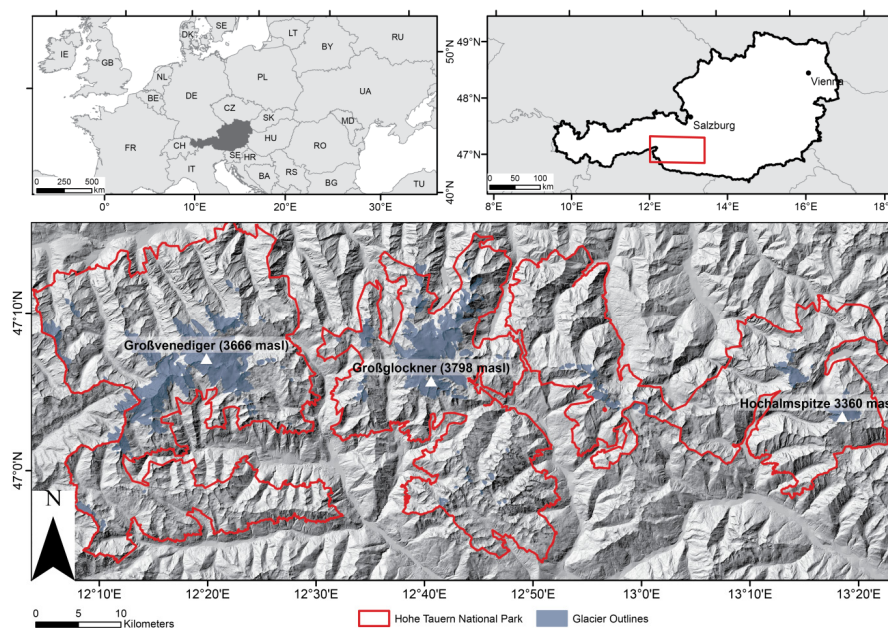

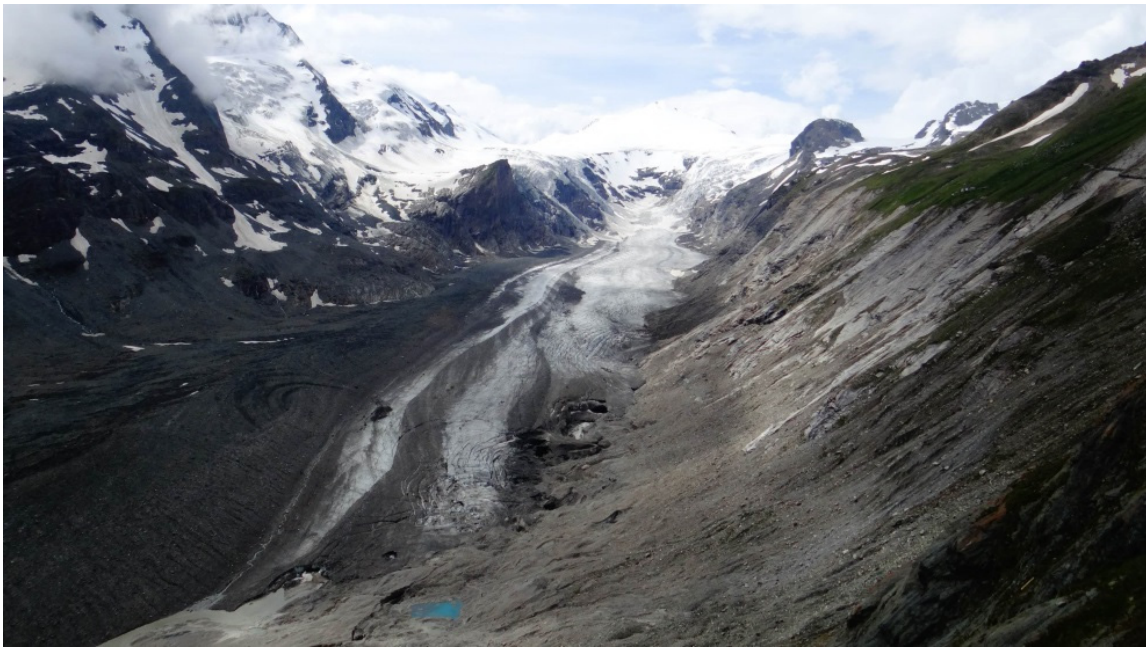**Figure 1.** Location map of Hohe Tauern National Park (HTNP) within Austria.

Figure 2. Pasterze Glacier, the largest glacier in Austria. Pasterze Glacier contains significant debris cover on the southern part of the glacier tongue. Photo: Hanna Siiki.

The climate in the Alps has changed considerably over the past decades [35]. The annual mean temperatures in the Greater Alpine Region have risen by about twice as much compared to average global warming or the average rise in the northern hemisphere since the late 19th century [36]. For example, the Sonnblick Observatory (3106 m a.s.l.) in the HTNP, which is the highest observatory in the world that is operated throughout the year, recorded an increase of approximately 2 °C since 1887 [37]. A major indicator of climate change in the Alps is the shrinkage and loss of volume of alpine glaciers with short response times [38].

One hundred and forty-five glaciers in HTNP were selected from the 1969 Austrian Glacier Inventory to assess glacier change; this was done to exclude snow patches and very small glaciers that were found in the AGI_1969. In total this represented 181 km^2 of the 207 km^2 (88%) of ice present in HTNP in 1969.

The data used in this study (Table 1) comprise three Landsat scenes from the end of the ablation season (late August/early September) of 1985, 2003, and 2013 as well as a LiDAR-derived DEM from between 2006 and 2013 resampled to 10 m resolution, which is freely available from the geodata portal of Austria (www.geoland.at). Although it could have been possible to obtain a 1 m DEM from this data, it is uncertain whether this large amount of data would have been stable within the eCognition software and it was unlikely to produce significantly better results. Ideally, DEM data from each time period would have been used in the classification. The SRTM DEM was available from February 2000, but it was found that the morphology of the glacier termini was not sufficiently prominent in the elevation model. This is suggested to be the result of the coarser 30 m resolution, meaning that a glacier of 500–600 m width would be only ~15 pixels, as well as the acquisition being in the accumulation season, when the glacier is more likely covered by snow. The LiDAR-derived DEM was therefore used as the elevation source for all three classifications as well as for generating the topographic derivatives (slope, curvature and aspect). The implications of this are discussed in Section 5.3. The change in elevation between the LiDAR DEM and the SRTM was used as a reference when manually correcting the 2013 outlines, along with an ALOS PALSAR coherence image (see Section 3.3). InSAR coherence data (commonly referred to in the literature simply as SAR coherence data) is an image generated from a pair of SAR images with a short interval between acquisitions. In our case we used two ALOS PALSAR images separated by approximately two weeks. The interferometric coherence between the

image pairs is used to determine which areas have undergone a change in surface conditions or motion, and which areas have been stable. This has been used by others to delineate where debris-covered ice is found [19,20].

Table 1. Data used in this study.

Scene ID	Date	Sensor	Resolution (m)
LC81920272013247LGN00	4 September 2013	Landsat 8	30 (15 pan-sharp)
LT51920272003236MTI01	24 August 2003	Landsat 5	30
LT51920271985234KIS00	22 August 1985	Landsat 5	30
	2006–2013	LiDAR	10
SRTM1N47E012V3	11 February 2000	SRTM	30
Track 637 Frame 930	01 July 2007	ALOS PALSAR	16 m × 13 m, geo-coded to 1 arc-second (~30 m)
Track 637 Frame 930	16 August 2007	ALOS PALSAR	16 m × 13 m, geo-coded to 1 arc-second (~30 m)

We used the SAR coherence data from 2007 only for data verification for two reasons: (1) because the size of glaciers in the Austrian Alps compared to the Himalayas makes SAR coherence data less suitable; and (2) we wanted to focus on assessing the potential of solely using high-resolution topographic data to classify debris covered ice based on the surface morphology.

3. Methods

Three classifications were performed within Trimble eCognition 9.0 for the years 1985, 2003 and 2013. Before analysis, all data were re-projected to UTM zone 33N. Image segmentation is one of the most critical stages in OBIA. As such, time was taken to find suitable segmentation parameters based on statistical pre-evaluations; this was done with the help of the Estimation of Scale Parameter 2 (ESP 2) tool [39]. In addition to choosing what datasets should be used to segment the data and create objects, scale, shape and compactness parameters are also specified. Within the multiresolution segmentation in eCognition, the scale parameter determines the size of the segmented image objects, the shape parameter dictates the relative importance of the shape versus the color/pixel values (calculated from the perimeter divided by four times the square root of the area) while the compactness decides how compact or smooth the final objects should be. eCognition calculates the compactness as the length and width divided by the area [40].

Running multiple hierarchical multiresolution segmentations was found to help group non-glacier objects together (Figure 3). Two segmentations were run before clean ice was classified, while an additional segmentation to create larger objects was performed before classifying debris-covered ice (see Table 2). The transient snowline (TSL) was mapped using a spectral difference segmentation performed on the second segmentation level (Table 2). A compact ruleset was applied that assigned objects to the classes of snow, clean ice or debris-covered ice. In order to account for the differences in bit depth between the Landsat 5 (8 bit–256 values) and Landsat 8 images (16 bit–65536 values), the thresholds for classifications had to be altered slightly. This was particularly important for thresholds for singular spectral bands, such as the red channel being used to map debris-covered ice. Fuzzy thresholds help alleviate this problem. Following image segmentation, objects were classified. This was done by assigning thresholds and fuzzy thresholds to the different classes, as detailed below.

Table 2. Parameters used in image segmentation. The clean ice was classified at level 2, the TSL was classified at level 2B, debris-covered ice was classified at level 3.

Segmentation Level	Scale Parameter	Shape	Compactness	Bands Used	Purpose
1	3 (5 *)	0.3	0.6	Blue, Green, NIR, Red, Slope, SWIR 1, SWIR 2, Thermal	Input for level 2
2	5 (8 *)	0.8	0.6	Blue, Green, NIR, Red, Slope, SWIR 1, SWIR 2, Thermal	Classifying clean Ice
2B	Maximum spectral difference = 10	n/a	n/a	NIR	Classifying transient snowline
3	10 (12 *)	0.25	0.5	NIR, Red, Slope, NDVI, canny edge detection (slope) **	Classifying debris covered Ice

*—Due to the increased bit depth, the scale parameter had to be increased for Landsat 8; **—As the topographic data did not correspond well to the 1985 data, the edge detection was not included in this classification.
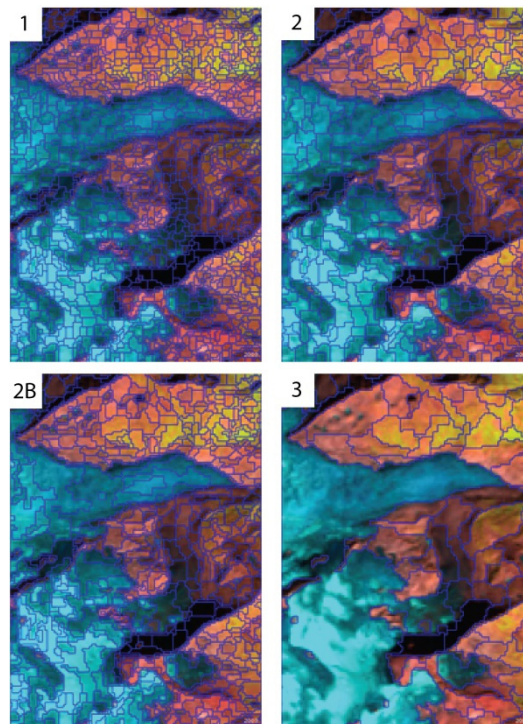

Figure 3. An illustration of the four segmentation levels within eCognition that were used within the classification procedure. An overview of each level and what it was used for is given in Table 2.

3.1. Clean Ice and Transient Snowline (TSL)

Clean ice was classified based on the following rules outlined below. Literature was used to select thresholds and is given when applicable; in other cases, the thresholds were found by trial and error. Note that many thresholds are fuzzy thresholds, and therefore contain a range of values (denoted with a dash). For example ⩾1.4–2 means objects were classified if they had values greater than 2, although if other criteria were met, objects with values between 2 and 1.4 were also considered. This allowed a degree of flexibility with the classification procedure.

- NIR/SWIR1 ratio ⩾1.4–2 (after [41,42])
- The Normalized Difference Snow Index (NDSI) with a threshold of ⩾−0.05–0.1 (after [43])

- The Normalized Difference Water Index (NDWI) with a threshold <0.15–0.4. It has been highlighted by others that turbid proglacial meltwater can be misclassified as clean ice (for example [4]), and the NDWI was therefore used to exclude proglacial lakes.
- Constraints of altitude of $\geqslant$2000 m and an upper threshold for the slope between 40° and 60°.

  - The classified image objects that bordered each other were then merged and clean ice smaller than 0.02 km^2 was removed from the classification.

Before the TSL could be classified, a spectral difference segmentation was performed. In this process, image objects already classified as clean ice were merged based on the similarity in spectral values (in this case the NIR spectral band), provided that neighboring objects did not vary in NIR reflectance by more than 10 (or 1000 for Landsat 8). The image objects then roughly corresponded to the boundary between snow and clean ice. It was found that the boundary between snow and ice was clearly visible using a false color composite image of the SWIR1, NIR and Red bands. An intensity image for these three bands was therefore generated with values ranging from 0 to 1. A threshold of 0.5 (or 0.38 for Landsat 8) was used to separate snow from clean ice.

3.2. Debris-Covered Ice

Due to the spectral similarity of debris-covered ice to the surrounding terrain, the classification procedure could not rely solely on spectral information. Instead, a combination of topographic parameters from the LiDAR DEM as well as the thermal band was used to delineate debris-covered ice. A canny edge detection process was used on the surface slope (Figure 4), which helped highlight where a break in the surface morphology occurred. This edge detection layer was then used in the segmentation when creating object level 3. The resulting image objects were then classified with a combination of fixed thresholds and fuzzy thresholds.

- -0.05–$0 \leqslant$ NDVI values $\leqslant 0.01$–0.03. The NDVI has been used by others to take advantage of the fact that debris-covered ice typically has less vegetation than the surrounding non-glacierized terrain (for example [24]).
- Red channel $\leqslant 59$ (in the case of Landsat 8, 11000 was used). This was found to be useful in excluding some paraglacial slopes.
- An upper threshold of the slope between 12° and 20°. Surface slope has been extensively used to delineate debris-covered ice, with a threshold of 20° being used previously in the European Alps (for example, see [18])
- Thermal band $\leqslant 12$ °C. The thermal signature has often been used to differentiate debris-covered ice (for example, see [17]). The strength of the thermal signature is, however, highly dependent on the thickness and distribution of the glacier debris [44] and care should be taken to not overly rely on the thermal signature. For this reason it was an advantage to include the thermal band as a fuzzy membership function. That way objects that met all other criteria yet did not have a distinct thermal signature could still be considered debris-covered ice.
- Normalized Difference Water Index (NDWI) $\geqslant -0.03$. A threshold in the NDWI was included to exclude marginal glacial lakes from the classification.

The classification was then expanded into neighboring objects ($\geqslant$80% shared border) that had a temperature of $\leqslant 10$ °C, or objects within 50 m of clean ice and 800 m from debris-covered ice that were spectrally similar and that had slopes of 20°–30°. Image objects that were initially classified as debris-covered ice but that did not border clean ice were then removed. Clean ice and debris-covered ice were finally combined into one class and any objects smaller than 0.1 km^2 or with very irregular shapes (compactness of objects $\geqslant$2.5) were removed, although during manual corrections some small glaciers that were present in the reference datasets were included.
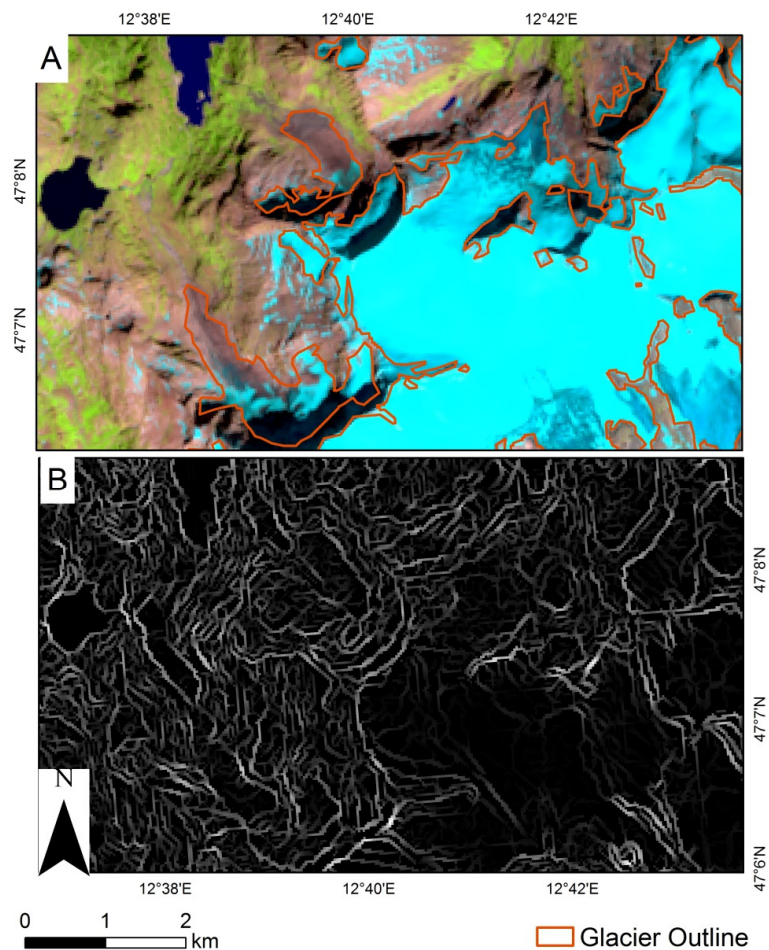
Figure 4. Edge detection on the LiDAR-derived DEM was effective for identifying debris-covered termini based on a break in surface morphology. (**A**) Shows the Landsat 2013 image with glacier outlines overlaid; (**B**) shows the edge detection dataset. It can be seen that the edge detection can be used in helping delineate the extent of debris-covered ice. The glacier outlines shown are the manually corrected 2013 outlines (2013_Man).

3.3. Post-Processing

The glacier outlines were smoothed using pixel-based growing and shrinking tools within eCognition before being exported as shapefiles. The glacier outlines were then divided by their drainage divides; the same drainage divides as the AGI were used to maintain consistency. Individual glacier shapefiles from the three OBIA classifications (1985_OBIA, 2003_OBIA and 2013_OBIA) were then compared with the AGI data from 1969 and 1998.

3.4. Manual Delineation and Accuracy Assessment

The reference glacier outlines available through GLIMS were dated from images acquired in 2003. Hence, in order to assess the accuracy of the OBIA_2013 outlines, it was necessary to create a set of manually corrected outlines (2013_Man) that were assumed to be "truth." These outlines were created with the aid of different data sources (Figure 5), namely Google Earth imagery, SAR coherence data, the profile curvature and hillshade models from the LiDAR DEM, and the difference in elevation between the LiDAR DEM and the SRTM DEM (henceforth referred to as difference in elevation, or ΔH). The comparison between these two DEMs meant that the spatial resolution of the LiDAR DEM (10 m) had to be reduced to the spatial resolution of the SRTM (30 m). This understandably results in a loss of information; however, since ΔH was only used for visual analysis and not quantitatively,

we do not consider this a particular problem. The reason for using ΔH was that glacier ice, even if debris-covered, is recognizable from the surrounding terrain by a change in surface elevation [42].
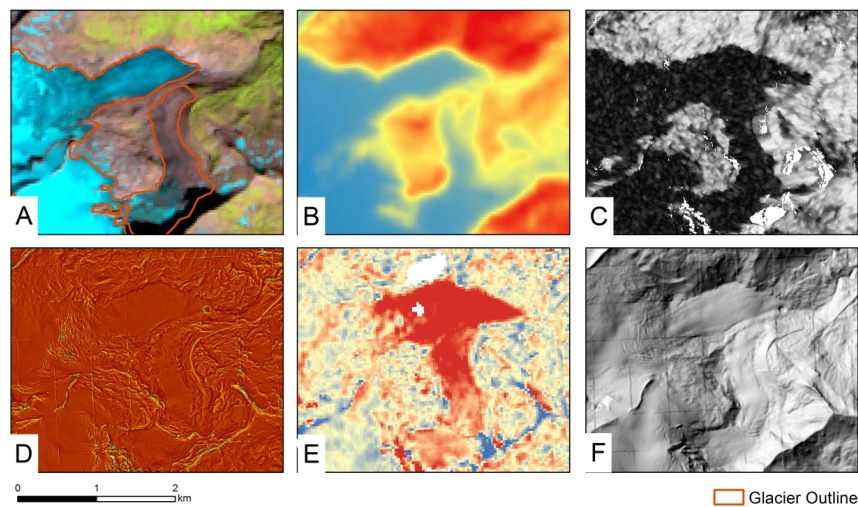

Figure 5. The glacier outlines (**A**) were manually corrected with reference to thermal data (**B**); SAR coherence data (**C**); the profile curvature (**D**); difference in elevation between 2000 and 2006 (**E**); and a hillshade model (**F**).

We evaluated the accuracy of our classifications in two ways. Firstly, we calculated simple percentage deviations (between OBIA_2003 and 2003_GLIMS, and OBIA_2013 and Man_2013 respectively). Although this is not a highly sophisticated method for assessing the accuracy of an image classification, it is widely used within the field of glaciology (for example [18,45]). In addition we assessed the accuracy using a confusion matrix following the methodology described by [46]. Ten thousand random points were generated within the HTNP and were assigned to either be "glacier" or "non-glacier" using the 2013_Man outlines. These points were then compared with the OBIA_2013 results and the following error terms were determined:

- User's accuracy—This is an error of commission and shows the percentage of the final classification that was a glacier.
- Producer's accuracy—This is an error of omission and describes the percentage of actual glacier area that was successfully classified.
- Overall accuracy—This considers both the user's accuracy and the producer's accuracy and shows the percentage of points that were correctly classified.
- Kappa coefficient—This is a measure of agreement between the classifications and the ground truth pixels, and of the classification not being due to random chance [47].

4. Results of Glacier Mapping

A total of 145 glaciers were mapped, representing 88% of the ice within HTNP in 1969. The results of the mapping are shown in Table S1. The most recent classification (OBIA_2013) contains 120 km^2 of ice. The average glacier size was 0.22 km^2 with 33 glaciers (23% of total) being larger than 1 km^2 and three glaciers (2%) being larger than 5 km^2. Supraglacial debris is present on four glaciers, most prominently on the Pasterze Glacier (1.1 km^2) and Schlaten Kees Glacier (0.95 km^2).

4.1. Decadal-Scale Changes in Glacier Area

Between AGI_1969 and OBIA_1985 there was a 3% decrease in glacier area from 181 km^2 to 175 km^2 with a mean loss of 0.4 km$^2 \cdot$ a^{-1}. This rate of glacier loss increased to 1.2 km$^2 \cdot$ a^{-1} between OBIA_1985 and AGI_1998 as the total glacier area decreased by a further 9% to 160 km^2. An increase

in the rate of glacier shrinkage happened between AGI_1998 and OBIA_2003, when the glacier area was reduced by a further 28% to 115 km^2 at a rate of 8.9 km$^2 \cdot$ a^{-1}. In total this accounts for a loss in glaciated area of 36% since 1969. Between OBIA_2003 and OBIA_2013, a growth of 5% (9 km^2) was observed at a rate of 0.6 km$^2 \cdot$ a^{-1}. This is discussed in Section 5.1. In 1969, 69% of glaciers were smaller than 1 km^2, and this had increased to 80% by 2013 (Figure 6). Between 1969 and 2013, the glaciers in the HTNP lost a total of 60.4 km^2 (33%) of the glacier area at a mean rate of 1.4 km^2 per year within the HTNP. Between 1985 and 2013, the glacier area reduced by 54.6 km^2 (31%) (Figures 7–10).
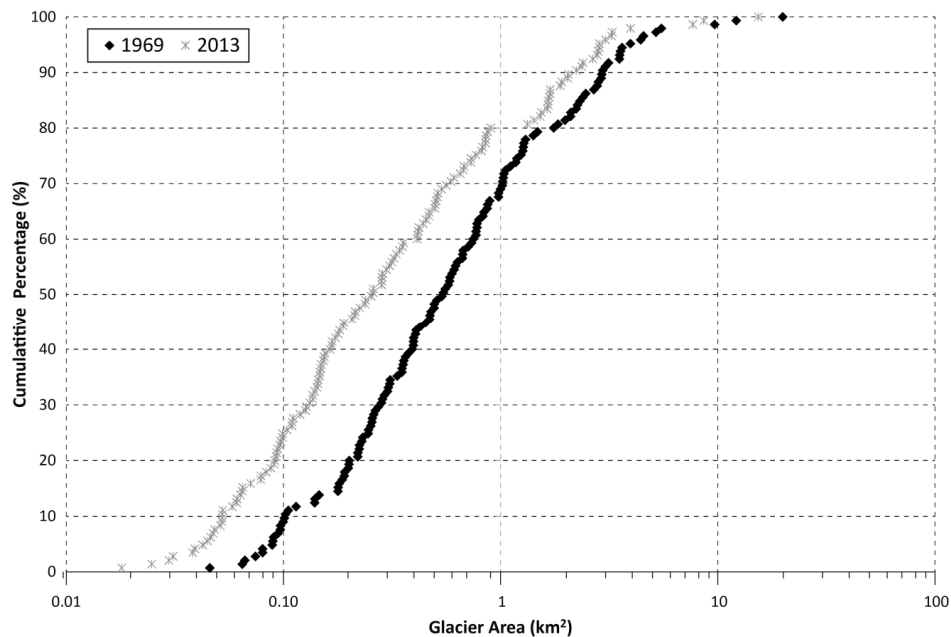

Figure 6. A cumulative distribution graph of the total glacier area against the size of individual glaciers in 1969 and 2013. Note that the x-axis is logarithmic.
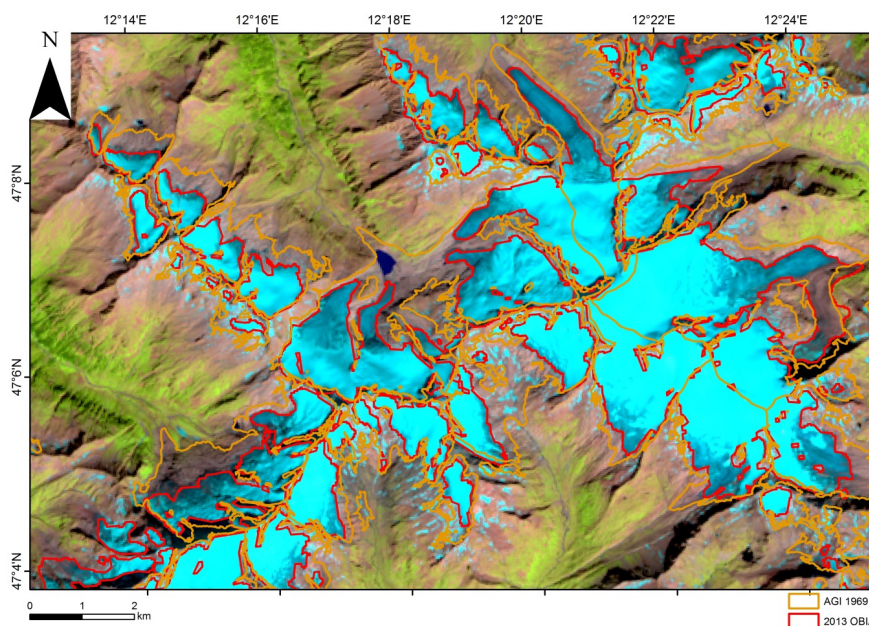

Figure 7. Total glacier area change between 1969 and 2013 over Schlaten Kees, Untersulzbach Kees, Viltragen Kees and Obersulzbach Kees. The background image is a false color (SWIR1, NIR, Red) Landsat image in order to help highlight snow and ice.
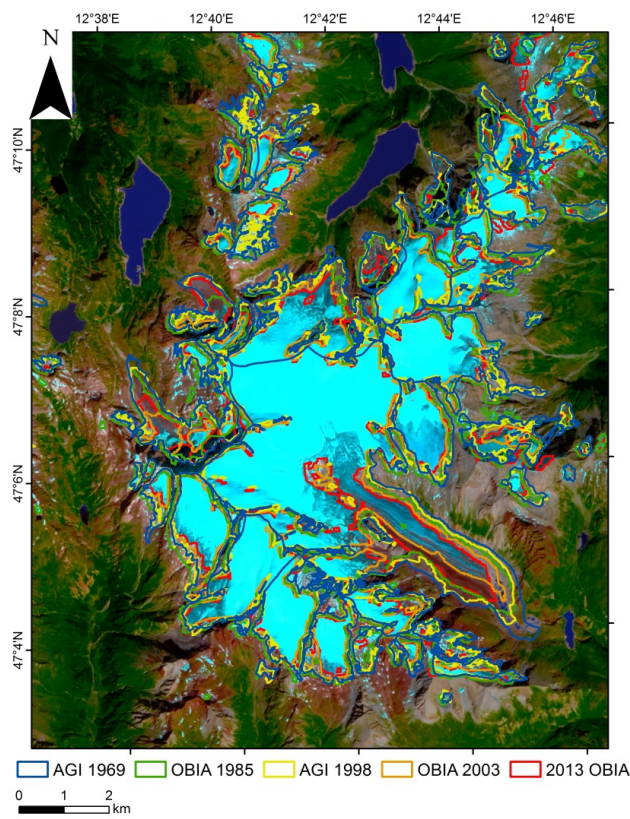
Figure 8. Decadal changes around Großglockner, including the largest glacier in Austria, the Pasterze Glacier, which includes a heavily debris-covered glacier tongue. The background image is a false color (SWIR1, NIR, Red) Landsat image in order to help highlight snow and ice.
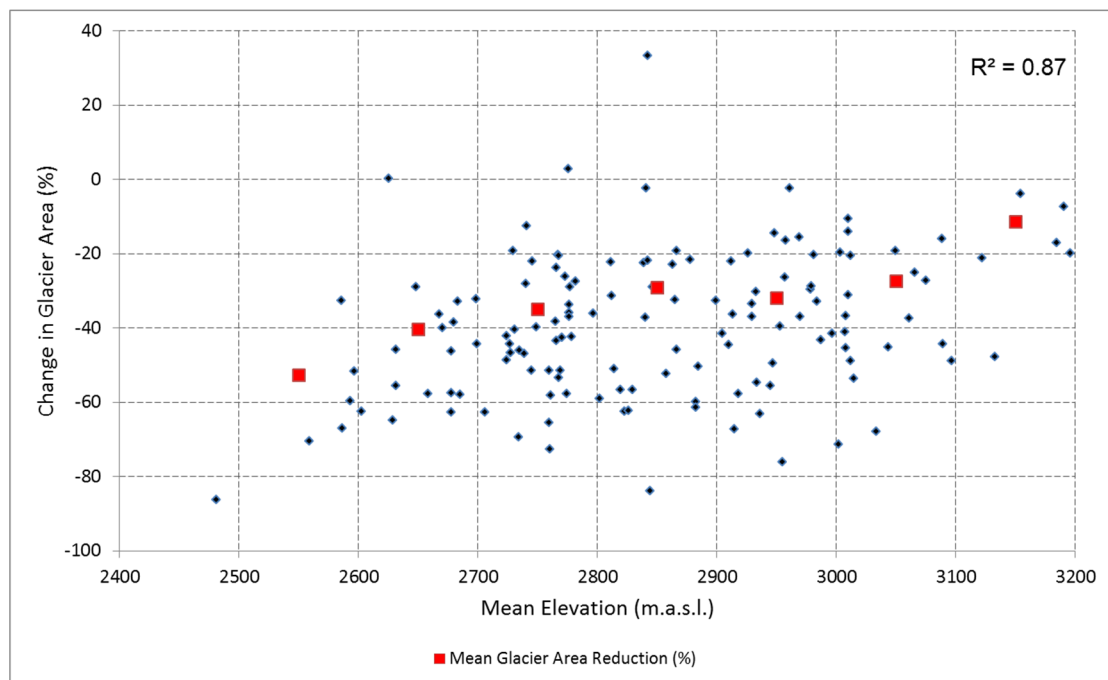

Figure 9. Percentage change in glacier area between 1969 and 2013 against mean glacier elevation.
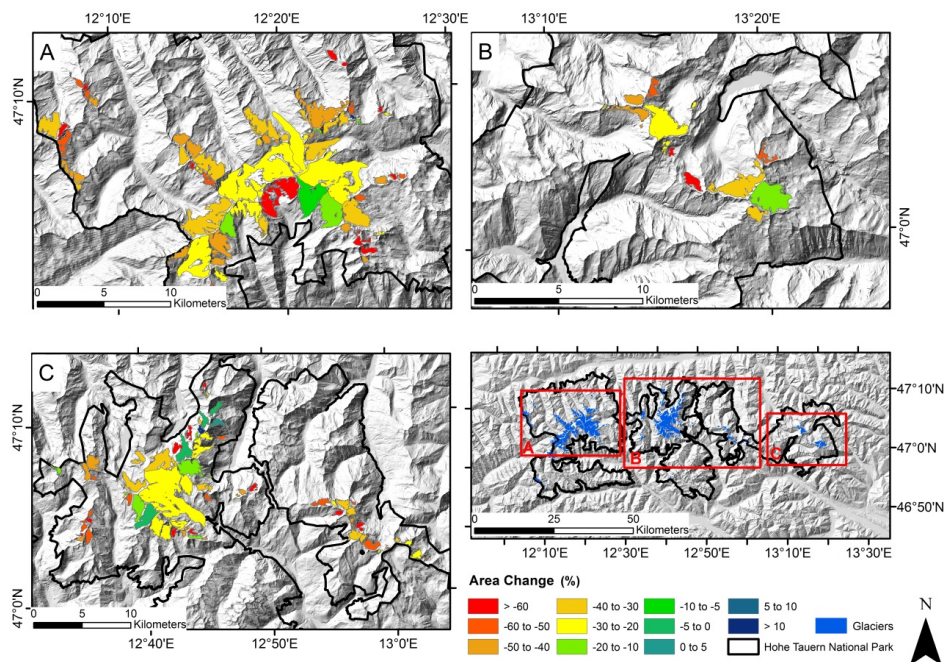
Figure 10. Percentage area change between 1969 and 2013 for individual glaciers within Western (**A**); Central (**B**); and Eastern (**C**) portions of the Hohe Tauern National Park.

Some relationship exists between mean glacier altitude and the change in glacier area ($R^2 = 0.87$), with glaciers at lower altitudes losing larger proportions of their area than glaciers lying at higher altitudes (as shown in Table S2 and Figure 9). The 16 glaciers with mean altitudes of <2600 m lost, on average, 53% of their area between 1969 and 2013, compared to the 29 glaciers between 3000 and 3100 m or the six glaciers higher than 3100 m which lost, respectively, 27% and 12% of their area. Three of these glaciers appeared to have grown in size. These snow patches (<0.08 km^2) are, however, located at relatively high altitudes, indicating that these area growths are most likely artefacts of seasonal snow. Smaller glaciers lost, on average, a greater proportion of area relative to their size than larger glaciers ($R^2 = 0.60$) (see Table S3 and Figure 11). The 69 glaciers with sizes <0.5 km^2 lost, on average, 55% of their area between 1969 and 2013, although there is a large spread in the data. Three glaciers lost >75% of their area (IDs: 5070 (Klockerin Kees), 6063 (Mailfrosnitz Kees) and 6052 (Dorfer Kees)). One glacier remained at a constant area (5058 (Walcher Kees)), while three underwent expansions of between 3% and 33% (IDs: 5056 (Sandboden Kees), 5068 (Kaindl Kees) and 6082)). Glaciers that were between 5 and 10 km^2 and >10 km^2, in contrast, lost an average of 25% and 24% of their areas, respectively. Glaciers which had a mean aspect towards the west-northwest (WNW) and south-southeast (SSE) lost slightly more area than glaciers facing in other directions (Table S4 and Figure 12). The difference, however, is not especially prominent at the regional level where glacier losses are more apparent on smaller glaciers, regardless of aspect (Figure 10).

It is hard to assign any general trends to how the debris-covered portions of glaciers have changed (Table S5), especially given that the classifications relied partly on one DEM from between 2006 and 2013. Nevertheless, changes to the spectral properties of the debris cover allowed the classification procedure to map some changes in the area of the debris cover. The reliability of these changes is discussed in Section 5.3. Information about the proportion of supraglacial debris is available from the three OBIA classifications, but not from the two AGIs. The five glaciers that have debris cover shrank by a mean of 22%, although the amount of debris cover varied. This is less than the mean reduction of 32% that occurred to glaciers within HTNP. While the amount of debris-covered ice on Ödenwinkel Kees was reduced by 42%, and Obersulzbach Kees lost all of its supraglacial debris, and three glaciers (Schlaten Kees, Unterer Riffl Kees and Pasterze Glacier) experienced an increase in debris-covered ice of 39%, 45% and 22%, respectively. Figures 7, 8 and 10 show the decadal-scale changes.
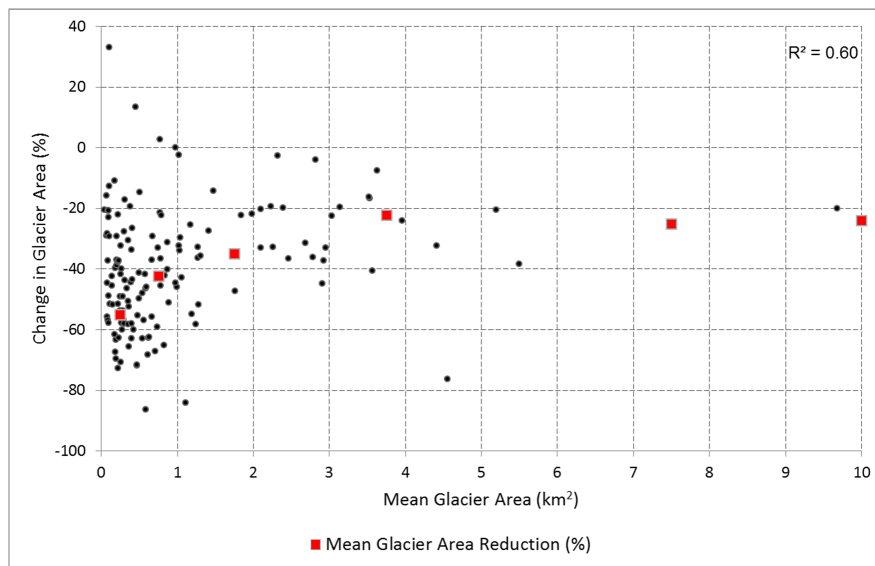
Figure 11. Percentage change in glacier area between 1969 and 2013 against glacier area as of 1969. Note that the two largest glaciers are excluded.
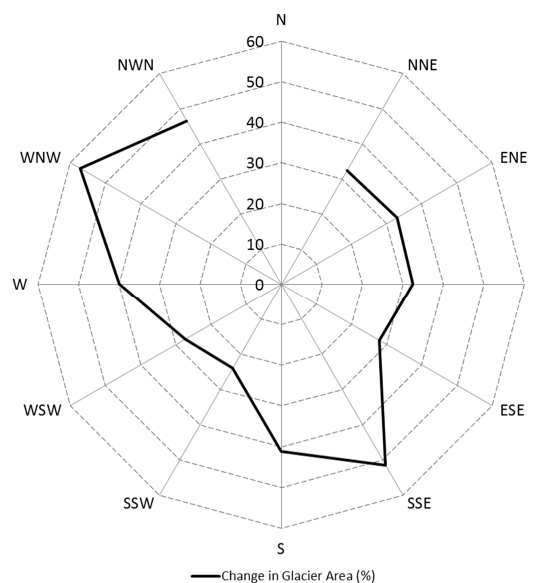

Figure 12. Percentage change in glacier area between 1969 and 2013 against mean glacier aspect. Note that no glaciers had a mean aspect towards the north (345°–15°).

4.2. Change in Transient Snowline Elevation (TSL)

Fifty-seven glaciers were larger than 0.2 km² and had the TSL mapped in both the 1985 and 2013 images, 47 of which also had the TSL mapped in the 2003 image. The TSL itself varies considerably over the region (Table S7 and Figure 13). The TSL varies by up to 199 m in elevation across the glaciers on the 1985 image, and up to 108 m on the 2013 image (Figure 14). Glaciers with the highest TSLs are those located on southerly exposed slopes (Table S8 and Figure 14), with glaciers facing the south and south-southwest having mean TSL altitudes in 1985 of 2910 and 2900 m compared with glaciers facing north-northeast (NNE) and north-northwest (NNW) which had altitudes of 2774 and 2814 m, respectively. Note that there is a lack of data on glaciers with a northerly aspect due to shadows. This is further discussed in Section 4.3. Given the variation of TSL elevation within HTNP it is not

straightforward to report changes over the entire region between the three classifications. However, the average altitude of the TSL in 1985 was 2913 m. This increased by an average of 159 m to 3071 m in 2003, leaving very little snow on most of the glaciers before decreasing by 66 m to 3005 m in 2013. In total, this represents a rise of 92 m between 1985 and 2013.
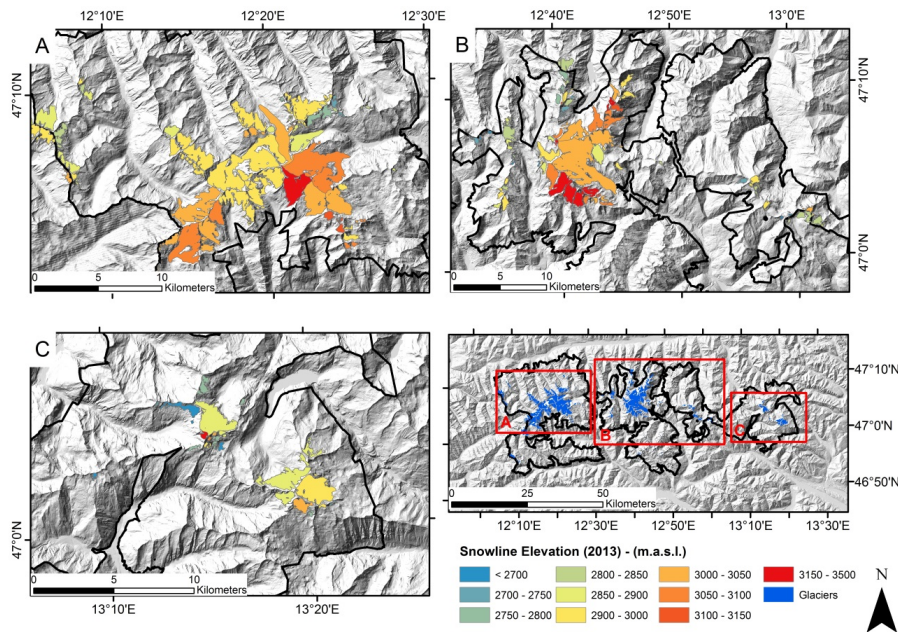

Figure 13. Snowline elevation as mapped for individual glaciers in 2013 within within Western (**A**); Central (**B**); and Eastern (**C**) portions of the Hohe Tauern National Park.
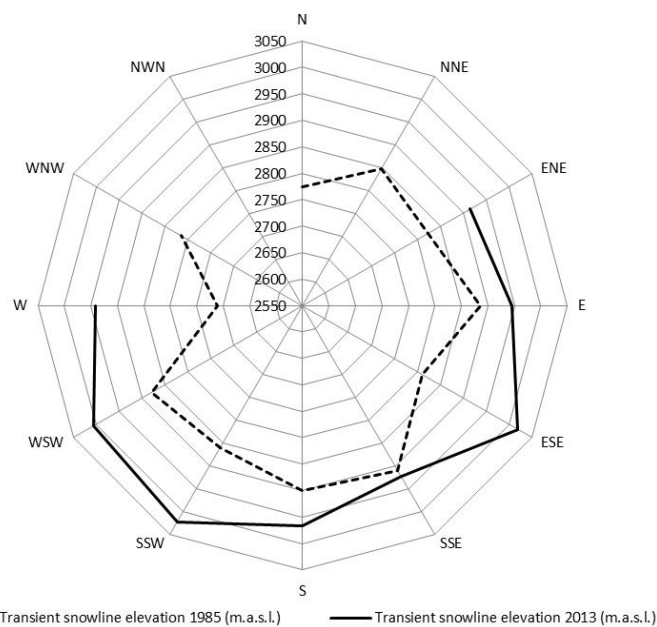

Figure 14. Mapped transient snowlines (TSLs) from 1985 and 2013 against aspect. Note that no snowlines were mapped with NWN aspects in 1985 or NWN and WNW in 1985, and these glaciers were more effected by shadows which masked the TSL.

4.3. Accuracy Assessment

In order to determine the accuracy of our OBIA classifications, we compare our glacier outlines with reference data (Table S6). Our OBIA_2003 outlines were compared with the GLIMS outlines [4], referred to henceforth as GLIMS_2003. OBIA_2013 outlines were compared with manually corrected outlines (2013_Man, Section 3.3). Although in many cases there is no alternative measure to assess classification accuracies, care needs to be taken when basing accuracy assessments on percentage differences to reference data, particularly between different studies that focus on different samples of glaciers. The relative accuracy is dependent on both the size of the glaciers and the total study area. As the study area or number of glaciers being mapped increases, the error term becomes more random and less systematic [45].

By comparing the total mapped ice for the 145 glaciers within HTNP, the OBIA_2003 classifications had an accuracy of 94% compared with GLIMS_2003. Among these, 62% of the glaciers were mapped with an accuracy of >90%, 39% of which were mapped with an accuracy of >95%. There were some glaciers identified in GLIMS_2003 that were not mapped in our classification. This was either due to the glaciers being smaller than the area threshold specified within the OBIA classification procedure, or because of shadows. The OBIA_2013 glacier outlines were mapped to a mean accuracy of 98%, 51% of the glaciers were mapped with an accuracy of >90% and 33% were mapped with an accuracy of >95%. The errors associated with the mapping of these glaciers are mainly caused by shadows and seasonal snow. In these cases these errors could mask changes in glacier area, and manual correction is necessary. For many of the glaciers, though, especially the larger glaciers, the glacier outlines were sufficiently accurate to see changes in glacier area over a decadal scale. It could be, however, that for annual changes in glacier area it is necessary to manually correct glacier outlines for shadow, snow and debris.

We also computed a confusion matrix for assessing the accuracy of OBIA_2013 (Table 3). The high kappa value shows that the classification did not happen due to chance. The user's accuracy shows that there were few false positives (objects mapped as glacier ice that in actuality were not), but the producer's accuracy shows that the classification was affected by false negatives (*i.e.*, glacier ice that was not mapped). This is mostly due to problems such as shadows, seasonal snow, and the difficulty of mapping debris-covered ice.

Table 3. User's accuracy, producer's value and overall accuracy from a confusion matrix. The values were determined for the OBIA classifications of glaciers in 2013, assessed against the manually delineated outlines (Man_2013).

User's Accuracy	Producer's Accuracy	Overall Accuracy	Kappa
94.1	81.6	0.98	0.9

The reference data contained no information that distinguished between clean ice and debris-covered ice. The entire region contained only 2.2 km^2 of glacial debris (1.8% of the total glacierized area). Nevertheless, if 2013_Man is compared to OBIA_2013 for just the debris-covered portions of the glaciers, then a total accuracy of 86.6% can be stated. Although given that just four glaciers had supraglacial debris, we maintain that it is more appropriate to consider the mapping of glacier accuracy over the entire glacier rather than report separate accuracies for clean ice and debris-covered ice. The accuracy of the debris-covered mapping for the 2003 and 1985 classifications is most likely lower than for the 2013 classification, given that the input data (Landsat data and LiDAR DEM) were not temporally consistent. This most likely explains the variations in the depicted debris cover between the three classifications (Table S5). We therefore consider our mapping of glacier debris in 2013 to be a fairly accurate assessment, but have less faith in the temporal trends in the supraglacial debris depicted.

In terms of the accuracy of our time series of decadal-scale change, several error terms must be considered in addition to the classification accuracy. The 2013 image is slightly affected by seasonal snow at higher elevations, which can cause an exaggeration of the glacier extent. Additionally, the 1998 glacier inventory (AGI_1998) is based on images from 1996 to 2002, making it harder to compare to the other results.

The extraction of the TSL altitude relies on the accuracy of the DEM used in extracting the snowline altitude. We used a 10 m DEM derived from LiDAR campaigns between 2006 and 2013 for extracting the snowline elevation for all three classifications. Although it can be assumed since the snowline approximately equals the annual equilibrium line, elevation changes here should be less than in the ablation area, and this needs to be kept in mind when interpreting results. The choice of satellite imagery also impacts the mapping of the TSL. Although the images we used were mostly snow-free, some northern-facing glaciers were obscured by shadows, making it impossible to map the TSL. Without *in situ* data (such as that used by [48] when working on changing snow and ice faces), it is difficult to thoroughly assess the accuracy of the TSL mappings, also if considering the high variability of TSL altitude within HTNP.

5. Discussion

5.1. Area Loss Compared with Other Areas in the European Alps

The glacier losses that we mapped within HTNP have been compared to other studies in the European Alps. It should be noted that small-scale glacier advances have been reported between the 1960s and 1980s [1,49]. It may have been possible to better assess such glacier variations; however, between the available datasets of 1969 and 1985, only a modest reduction in glacier area is visible. Paul *et al.*, (2011) found an approximate reduction in glacier area of 33% over the Austrian, French, Italian and Swiss Alps between 1970 $\pm$ 15 years and 2003. This corresponds well with our results of a decrease in 33% between 1969 and 2003 or 31% between 1985 and 2013. Carturan *et al.* (2013) found a 23.4% $\pm$ 3% reduction in glacier area between 1987 and 2009 in the Ortles-Cevedale Alps of Italy, while Gardent *et al.* (2014) found a 25% reduction in area between the late 1960s and the late 2000s in the French Alps. This is less than the 31% we found between 1985 and 2013.

Abermann *et al.* (2009) found an 8.2% reduction in area between 1997 and 2006 in the Austrian Ötztal Alps, considerably less than the 24% reduction we found between 1998 and 2003. Paul *et al.* (2011) found a reduction of 18% in area for glaciers in the Swiss Alps between 1985 and 1999 [50], double the 9% reduction within HTNP between 1985 and 1998. This shows that there is a large spatial heterogeneity in glacier area response to climate across the European Alps, although an evident trend of a clear reduction in glacier size over the last decades is dominant.

A 5% increase in glacier area is found between 2003 and 2013. We have two explanations for this apparent anomaly. The 2013 image contained some seasonal snow at higher altitudes, and optical satellite imagery struggles to differentiate between snow and ice, so if seasonal snow obscures the glacier margin, automatic methods are prone to misclassify this as glacier growth. Additionally, the summer of 2003 was abnormally hot. The European heatwave of 2003 caused extreme glacier melt in the European Alps at a rate of eight times the long-term average (1960–2000), and double the rate experienced in the 1998 heatwave [51,52].

Pasterze Glacier, the largest glacier in Austria, contains two components, a northern, debris-free part, and a southern, debris-covered part [53]. Our results showed that between 1985 and 2013, the amount of debris cover on the Pasterze Glacier increased by 22% to 1.1 km^2. It should, however, be noted (as discussed in Section 5.3) that without corresponding elevation data, delineating debris-covered ice is difficult. This can lead to some erroneous results, such as the amount of debris in 2003 being less than in 1985 and 2013. Nevertheless, Kellerer-Pirklbauer (2008) found a 40% increase in the amount of debris between 1970 and 2008, which is in line with our findings.

5.2. Use of OBIA for Glacier Mapping

By using OBIA we were able to map 120 km^2 (as of 2013) of glacier ice, including both debris-covered ice and clean ice, semi-automatically. OBIA offered many advantages over PBIA techniques when applied to glacier mapping. Rastner *et al.* [22] highlight how OBIA provides marginally higher (~3%) accuracies for mapping clean ice when compared to PBIA. Accuracy is, however, not the only advantage of OBIA. OBIA allows classes to be defined by multiple characteristics, and this allows, for example, proglacial lakes to be separated from glacier ice (a problem identified by Andreassen *et al.* [54]) by including a classification threshold based on the NDWI in the ruleset. Working at the object level additionally allows some post-processing to be included in the workflow, for example smoothing object boundaries or eliminating some false-positive objects. This allowed snow patches to be removed by size, mean elevation and shape, as well as removing debris-covered ice that is not attached to clean ice. Snow patches can be a problem when comparing classification results with old glacier inventories. OBIA allows the inclusion of vector data, allowing only ice masses that were present in the glacier inventory to be delineated in the classification. This can help reduce the amount of false positives that need to be removed with opportune post-processing.

OBIA offers significantly more advantages when applied to mapping debris-covered ice. Debris-covered ice is difficult to identify based solely on spectral information [55,56], thereby additional data sources such as a DEM or SAR coherence data should be used. OBIA allows these data sources to be combined in the classification procedure. In this study we used the surface morphology, spectral values and thermal properties to identify debris-covered ice. The morphology was used by performing an edge extraction on the surface slope; this edge detection was then used in the segmentation of image objects. This analysis could have been done using PBIA, but edge detection could have only been used as a guide to manual interpretation as opposed to being a component in a semi-automated workflow. Once the ruleset was generated for one scene, it could be applied to other imagery from different dates, although due to changes in the sensor (Landsat 8 *vs.* Landsat 5) or differences in the time of acquisition or scene illumination, small adjustments had to be made to the thresholds used in the classification. The transferability of rulesets highlights the potential for OBIA being used for creating more frequent and consistent glacier inventories.

The accuracy of semi-automated mappings of glacier ice is affected by a number of factors, such as the presence of seasonal snow, shadows or the presence of supraglacial debris [57]. Additionally, given the reported rapid shrinkage of glaciers in the European Alps, the range of years which the LiDAR data were gathered (2006 to 2013) contributes to the uncertainty of mapping the debris-covered glaciers.

The transient snowline proved relatively easy to map due to the spectral difference between bare ice and snow. Distinguishing between bare ice and snow is an established technique [48,58,59]. Our analysis, however, was limited by having just three years' worth of data. Although an overall rise in TSL is observable between 1985 and 2013, three TSL measurements are not sufficient to establish a temporal trend, given the large variability within each image. The 2003 dataset shows almost no snow being left on the glaciers. Although this makes it harder to infer a trend from the three datasets, this augmentation in TSL altitude most likely reflects the unusually hot summer of 2003 where extensive ablation occurred for a prolonged period of time [51]. The snowline varies spatially within HTNP, with glaciers that have a more southern aspect and therefore a higher radiation receipt being characterized by higher snowlines [60]. Care needs to be taken when interpreting snowlines mapped from optical imagery and interpreting them as a proxy for ELA. The mapped snowline is highly affected by the image acquisition date, seasonal snowfalls and shadow [15,58]. It is therefore of great importance that the satellite acquisition occurs as close as possible to the end of the ablation season in order for multiple images to be comparable. The images we used were acquired from the end of August or start of September, so it is likely that further ablation occurred between these dates and the period of first snowfall.

When snowlines are mapped over decadal timescales, then the snowline altitude can be used as a proxy for the ELA or glacier mass balance [61,62]. We, however, do not consider our snowline

time series to be sufficiently long to infer any changes in glacier mass balance. We instead consider our snowline mapping results to demonstrate the potential for semi-automatically delineating the transient snowline from time series of optical satellite images using OBIA.

We believe that OBIA is, therefore, a suitable methodology for semi-automated mapping of glaciers, including the delineation of debris-covered ice and the TSL. Once the classification rulesets had been created in eCognition, it took less than 5 min to fully classify the entire study area. The adjustments needed to adapt the rulesets for the different Landsat sensors took approximately 45 min before the classification could be run again on a different image. The results had an accuracy of 92%, meaning that only minor portions had to be manually edited. Once the classification ruleset has been generated, OBIA offers a method for relatively efficient transferability to other images.

5.3. Topographic Data for Debris-Covered Ice

Topographic data have been widely used to map debris-covered ice by interpreting a change in morphology at the glacier terminus [18,63,64]. To date, however, edge detection has not been used as a processing step within a classification of debris-covered ice. Although the morphology can be used to depict the glacier terminus edge, there is some discussion needed whether what can be detected as a break of topography is active glacier ice, or whether it is stagnant ice. Stagnant ice can become decoupled from the active flowing glacier ice [65]. However, it can still contribute to water resources through melting. There is no clear consensus on whether stagnant glacier ice should be mapped as part of the glacier, although with the exception of perhaps the Pasterze Glacier this is not of major concern in the HTNP, it must be considered when working in areas of significant supraglacial debris such as the Himalayas [66].

Edge detection proved a reliable method to extract the terminus position of debris-covered glacier tongues. Only one DEM dataset derived from LiDAR data acquired between 2007 and 2013 was available, meaning that a change in surface morphology could not be used to delineate changes in debris cover. The DEM was used to assist creating image objects for OBIA_2003 and OBIA_2013, but no DEM was available to correspond with OBIA_1985. This most likely explains the slightly dubious results obtained for the debris-cover mapping, for example the Pasterze Glacier experiencing a decrease and subsequent increase in debris cover. The classification procedure managed to depict changes in supraglacial debris by variations in the spectral values, although ideally each OBIA classification would have had a corresponding DEM in order to map changes in morphology at the glacier terminus. Future LiDAR acquisitions could be used to accurately determine the shrinkage of debris-covered glacier tongues on a multi-temporal basis by incorporating edge detection algorithms within the analysis. It is not possible, however, to differentiate between debris-covered ice and ice-cored moraines by solely using topographic data. It would therefore be advantageous for future work to incorporate either SAR coherence data or surface displacement data derived from feature tracking of multi-temporal satellite images [67].

6. Conclusions

We have demonstrated the use of Object-Based Image Analysis (OBIA) for robust mapping of clean and debris-covered ice within Hohe Tauern National Park, Austria. By comparing our three classifications (OBIA_1985, OBIA_2003 and OBIA_2013) with the two Austrian Glacier Inventories (AGI_1969 and AGI_1998) we have determined the total loss and rate of glacier terminus retreat for 145 glaciers. Mean rates of glacier loss appear to have increased from a mean of 0.4 $km^2 \cdot a^{-1}$ between 1969 and 1985 up to a rate of 8.9 $km^2 \cdot a^{-1}$ between 1998 and 2003, although given the time intervals we are working with, it is difficult to speculate that this represents an acceleration in glacier loss. Our analysis contained only five time periods over a 44-year period, one of which was hampered by seasonal snow. Care therefore needs to be taken in interpreting how the rate of glacier loss has changed over this time. It can be stated, however, that the total area of ice reduced by 33% from 181 km^2 in 1969 to 120 km^2 in 2013. The year 2003 is showed as having a total ice area of 5% less than in 2013 at

115 km^2. We explain this as being due to a combination of some seasonal snow at higher altitudes in the 2013 satellite image and the extreme heat of the summer of 2003.

While clean ice can already be robustly classified using PBIA methods, the inclusion of spatial and contextual information helps remove false positives (such as snow patches or turbid-water) and semi-automatizes post-processing procedures, thereby reducing the amount of manual corrections needed. Additionally, the transferability of rulesets could further the development of semi-automated glacier mapping procedures in other regions of the world.

The mapping of debris-covered ice can be greatly improved by using OBIA. Working at the object level allows topographic as well as spectral and thermal data to be used in combination to delineate debris-covered ice. Contextual and spatial information can be used to remove debris not connected to clean ice, or expand the classification into spectrally similar objects. Additionally, the inclusion of algorithms such as edge detection allow debris-covered ice to be mapped using breaks in surface morphology, building on the work of others [18,63,68].

The future availability of relatively high resolution DEMs, such as the TanDEM-X Global DEM or Sentinel-2 photogrammetric DEMs, could provide possibilities of using more up-to-date topographic data to map debris-covered ice [69,70]. In particular, the use of multi-temporal high-resolution stereo imagery, providing optical imagery and a DEM from the same acquisition, should be explored. Additionally, although we have demonstrated that the use of OBIA in classifying clean ice is efficient and accurate, the process still requires the careful selection of thresholds for band ratios and spectral indices. OBIA allows the use of "automatic thresholds" where a threshold is determined that divides a histogram into two subsets [71,72]. Such an approach has not been utilized within the field of remote sensing glaciology, and has the potential to facilitate a fully automatic workflow for the classification of clean ice. Given the prominent spectral signature of clean ice as opposed to fresh snow, future studies could also map the TSL using automatic thresholds over a long timescale, providing an automatically generated time series of transient snowline fluctuations.

Author Contributions: Benjamin Robson wrote the manuscript with contributions and feedback from all co-authors. The OBIA Analysis was carried out by Benjamin Robson and Daniel Hölbling with advice and guidance from Christopher Nuth. Tazio Strozzi obtained and processed the ALOS coherence data.

Conflicts of Interest: The authors declare no conflict of interest.

References

1. Zemp, M.; Paul, F.; Hoelze, M.; Haeberli, W. Glacier fluctuations in the European Alps, 1850–2000. *Darkening Peaks Glacier Retreat Sci. Soc.* **2008**. [CrossRef]

2. Fischer, A. Glaciers and climate change: Interpretation of 50 years of direct mass balance of Hintereisferner. *Glob. Planet Chang.* **2010**, *71*, 13–26. [CrossRef]

3. Fischer, M.; Huss, M.; Barboux, C.; Hoelzle, M. The new Swiss Glacier Inventory SGI2010: Relevance of using high-resolution source data in areas dominated by very small glaciers. *Arct. Antarct Alp. Res.* **2014**, *46*, 933–945. [CrossRef]

4. Paul, F.; Frey, H.; le Bris, R. A new glacier inventory for the European Alps from Landsat TM scenes of 2003: Challenges and results. *Ann. Glaciol.* **2011**, *52*, 144–152. [CrossRef]

5. Koboltschnig, G.R.; Schöner, W. The relevance of glacier melt in the water cycle of the Alps: The example of Austria. *Hydrol. Earth Syst. Sci.* **2011**, *15*, 2039–2048. [CrossRef]

6.　Schaefli, B.; Hingray, B.; Musy, A. Climate change and hydropower production in the Swiss Alps: Quantification of potential impacts and related modelling uncertainties. *Hydrol. Earth Syst. Sci. Discuss.* **2007**, *11*, 1191–1205. [CrossRef]

7.　Chiarle, M.; Iannotti, S.; Mortara, G.; Deline, P. Recent debris flow occurrences associated with glaciers in the Alps. *Glob. Planet Chang.* **2007**, *56*, 123–136. [CrossRef]

8.　Abermann, J.; Kuhn, M.; Fischer, A. Climatic controls of glacier distribution and glacier changes in Austria. *Ann. Glaciol.* **2011**, *52*, 83–90. [CrossRef]

9.　Lambrecht, A.; Kuhn, M. Glacier changes in the Austrian Alps during the last three decades, derived from the new Austrian glacier inventory. *Ann. Glaciol.* **2007**, *46*, 177–184. [CrossRef]

10.　Paul, F.; Haeberli, W. Spatial variability of glacier elevation changes in the Swiss Alps obtained from two digital elevation models. *Geophys. Res. Lett.* **2008**, *35*. [CrossRef]

11.　Berthier, E.; Vincent, C. Relative contribution of surface mass-balance and ice-flux changes to the accelerated thinning of Mer de Glace, French Alps, over 1979–2008. *J. Glaciol.* **2012**, *58*, 501–512. [CrossRef]

12.　Kääb, A.; Huggel, C.; Paul, F.; Wessels, R.; Raup, B.; Kieffer, H.; Kargel, J. Glacier Monitoring from ASTER Imagery: Accuracy and Applications. In Proceedings of the EARSeL-LISSIG-Workshop Observing Our Cryosphere from Space, Bern, Switzerland, 11–13 March 2002; pp. 43–53.

13.　Gardent, M.; Rabatel, A.; Dedieu, J.-P.; Deline, P. Multitemporal glacier inventory of the French Alps from the late 1960s to the late 2000s. *Glob. Planet Chang.* **2014**, *120*, 24–37. [CrossRef]

14.　Carturan, L.; Filippi, R.; Seppi, R.; Gabrielli, P.; Notarnicola, C.; Bertoldi, L.; Paul, F.; Rastner, P.; Cazorzi, F.; Dinale, R.; *et al*. Area and volume loss of the glaciers in the Ortles-Cevedale group (Eastern Italian Alps): Controls and imbalance of the remaining glaciers. *Cryosphere* **2013**, *7*, 1339–1359. [CrossRef]

15.　Mathieu, R.; Chinn, T.; Fitzharris, B. Detecting the equilibrium-line altitudes of New Zealand glaciers using ASTER satellite images. *N. Z. J. Geol. Geophys.* **2009**, *52*, 209–222. [CrossRef]

16.　Chinn, T.J.; Heydenrych, C.; Salinger, M.J. Use of the ELA as a practical method of monitoring glacier response to climate in New Zealand's Southern Alps. *J. Glaciol.* **2005**, *51*, 85–95. [CrossRef]

17.　Taschner, S.; Ranzi, R. Comparing the opportunities of Landsat-TM and Aster data for monitoring a debris covered glacier in the Italian Alps within the GLIMS project. In Proceedings of the 2002 IEEE International Geoscience and Remote Sensing Symposium, Toronto, ON, Canada, 24–28 June 2002; pp. 1044–1046.

18.　Paul, F.; Huggel, C.; Kaab, A. Combining satellite multispectral image data and a digital elevation model for mapping debris-covered glaciers. *Remote Sens. Environ.* **2004**, *89*, 510–518. [CrossRef]

19.　Frey, H.; Paul, F.; Strozzi, T. Compilation of a glacier inventory for the western Himalayas from satellite data: Methods, challenges, and results. *Remote Sens. Environ.* **2012**, *124*, 832–843. [CrossRef]

20.　Robson, B.A.; Nuth, C.; Dahl, S.O.; Hölbling, D.; Strozzi, T.; Nielsen, P.R. Automated classification of debris-covered glaciers combining optical, SAR and topographic data in an object-based environment. *Remote Sens. Environ.* **2015**, *170*, 372–387. [CrossRef]

21.　Blaschke, T.; Hay, G.J.; Kelly, M.; Lang, S.; Hofmann, P.; Addink, E.; Feitosa, R.Q.; van der Meer, F.; van der Werff, H.; van Coillie, F. Geographic object-based image analysis-towards a new paradigm. *ISPRS J. Photogramm. Remote Sens.* **2014**, *87*, 180–191. [CrossRef] [PubMed]

22.　Rastner, P.; Bolch, T.; Notarnicola, C.; Paul, F. A Comparison of Pixel- and Object-Based Glacier Classification With Optical Satellite Images. *IEEE J. STARS* **2014**, *7*, 853–862. [CrossRef]

23.　Bajracharya, S.R.; Maharjan, S.B.; Shrestha, F.; Bajracharya, O.R.; Baidya, S. *Glacier Status in Nepal and Decadal Change from 1980 to 2010 Based on Landsat Data*; International Centre for Integrated Mountain Development: Kathmandu, Nepal, 2014.

24.　Bajracharya, S.R.; Maharjan, S.B.; Shrestha, F. The status and decadal change of glaciers in Bhutan from the 1980s to 2010 based on satellite data. *Ann. Glaciol.* **2014**, *55*, 159–166. [CrossRef]

25.　Bajracharya, S.R.; Shrestha, B. *The Status of Glaciers in the Hindu Kush-Himalayan Region*; International Centre for Integrated Mountain Development (ICIMOD): Kathmandu, Nepal, 2011.

26.　Eisank, C.; Drăguţ, L.; Götz, J.; Blaschke, T. Developing a semantic model of glacial landforms for object-based terrain classification—The example of glacial cirques. *GEOBIA* **2010**, *XXXVIII-4/C7*, 1682–1777.

27.　Paul, F.; Arnaud, Y.; Ranzi, R.; Rott, H. European Alps. In *Global Land Ice Measurements from Space*; Kargel, J.S., Leonard, G.J., Bishop, M.P., Kääb, A., Raup, B.H., Eds.; Springer: Berlin, Germany; Heidelberg, Germany, 2014; pp. 439–463.

28.   Carinthia Regional Government. Digitales Geländemodell (10 m) Kärnten. Available online: http://data.ktn.gv.at/package/digitales-gelaendemodell-10m-kaernten/ (accessed on 14 October 2015).

29.   Tirol Regional Government. Digitales Geländemodell Tirol. Available online: https://www.tirol.gv.at/data/datenkatalog/geographie-und-planung/digitales-gelaendemodell-tirol/ (accessed on 28 March 2015).

30.   Salzburg Regional Goverment. Status Laserscan Befliegung im Bundesland Salzburg. Available online: http://www.salzburg.gv.at/als-status-jahr_2014_09_05.pdf (accessed on 28 March 2015).

31.   Abermann, J.; Lambrecht, A.; Fischer, A.; Kuhn, M. Quantifying changes and trends in glacier area and volume in the Austrian Ötztal Alps (1969–1997–2006). *Cryosphere Discuss.* **2009**, *3*, 415–441. [CrossRef]

32.   Schicker, I. *Changes in Area of Stubai Glaciers analysed by means of Satellite Data for the GLIMS Project*; University of Innsbruck: Innsbruck, Austria, 2006.

33.   Van Zyl, J.J. The Shuttle Radar Topography Mission (SRTM): A breakthrough in remote sensing of topography. *Acta Astronaut.* **2001**, *48*, 559–565. [CrossRef]

34.   Kellerer-Pirklbauer, A. The Supraglacial Debris System at the Pasterze Glacier, Austria: Spatial Distribution, Characteristics and Transport of Debris. *Z. Geomorphol. Suppl. Issues* **2008**, *52*, 3–25. [CrossRef]

35.   Gobiet, A.; Kotlarski, S.; Beniston, M.; Heinrich, G.; Rajczak, J.; Stoffel, M. 21st century climate change in the European Alps—A review. *Sci. Total Environ.* **2014**, *493*, 1138–1151. [CrossRef] [PubMed]

36.   Auer, I.; Bohm, R.; Jurkovic, A.; Lipa, W.; Orlik, A.; Potzmann, R.; Schoner, W.; Ungersbock, M.; Matulla, C.; Briffa, K. HISTALP-historical instrumental climatological surface time series of the Greater Alpine Region. *Int. J. Climatol.* **2007**, *27*, 17–46. [CrossRef]

37.   Behm, M.; Raffeiner, G.; Schöner, W. Climate change and possible impacts on alpinism: A case study on the Nationalpark Hohe Tauern. In Proceedings of the 3rd Symposium of the Hohe Tauern National Park for Research in Protected Areas, Kaprun, Austria, 15–17 September 2005; pp. 21–24.

38.   Schrott, L.; Otto, J.-C.; Keller, F. Modelling alpine permafrost distribution in the Hohe Tauern region, Austria. *Austrian J. Earth Sci.* **2012**, *105*, 169–183.

39.   Dragut, L.; Csillik, O.; Eisank, C.; Tiede, D. Automated parameterisation for multi-scale image segmentation on multiple layers. *Isprs J. Photogramm. Remote Sens.* **2014**, *88*, 119–127. [CrossRef] [PubMed]

40.   Trimble. *eCognition Developer Reference Book 9.0*; Trimble: Munich, Germany, 2014.

41.   Racoviteanu, A.E.; Paul, F.; Raup, B.; Khalsa, S.J.S.; Armstrong, R. Challenges and recommendations in mapping of glacier parameters from space: Results of the 2008 Global Land Ice Measurements from Space (GLIMS) workshop, Boulder, Colorado, USA. *Ann. Glaciol.* **2009**, *50*, 53–69. [CrossRef]

42.   Kääb, A.; Bolch, T.; Casey, K.; Heid, T.; Kargel, J.; Leonard, G.; Paul, F.; Raup, B. Glacier Mapping and Monitoring Using Multispectral Data. In *Global Land Ice Measurements from Space*; Kargel, J.S., Leonard, G.J., Bishop, M.P., Kääb, A., Raup, B.H., Eds.; Springer: Berlin, Germany; Heidelberg, Germany, 2014; pp. 75–112.

43.   Silverio, W.; Jaquet, J.-M. Glacial cover mapping (1987–1996) of the Cordillera Blanca (Peru) using satellite imagery. *Remote Sens. Environ.* **2005**, *95*, 342–350. [CrossRef]

44.   Mihalcea, C.; Brock, B.W.; Diolaiuti, G.; D'Agata, C.; Citterio, M.; Kirkbride, M.P.; Cutler, M.E.J.; Smiraglia, C. Using ASTER satellite and ground-based surface temperature measurements to derive supraglacial debris cover and thickness patterns on Miage Glacier (Mont Blanc Massif, Italy). *Cold Reg. Sci. Technol.* **2008**, *52*, 341–354. [CrossRef]

45.   Nuth, C.; Kohler, J.; König, M.; von Deschwanden, A.; Hagen, J.O.; Kääb, A.; Moholdt, G.; Pettersson, R. Decadal changes from a multi-temporal glacier inventory of Svalbard. *Cryosphere* **2013**, *7*, 1603–1621. [CrossRef]

46.   Beck, M.W.; Vondracek, B.; Hatch, L.K.; Vinje, J. Semi-automated analysis of high-resolution aerial images to quantify docks in glacial lakes. *ISPRS J. Photogramm. Remote Sens.* **2013**, *81*, 60–69. [CrossRef]

47.   Congalton, R.G. A review of assessing the accuracy of classifications of remotely sensed data. *Remote Sens. Environ.* **1991**, *37*, 35–46. [CrossRef]

48.   Bayr, K.J.; Hall, D.K.; Kovalick, W.M. Observations on glaciers in the eastern Austrian Alps using satellite data. *Int. J. Remote Sens.* **1994**, *15*, 1733–1742. [CrossRef]

49.   Patzelt, G. The period of glacier advances in the Alps, 1965 to 1980. *Z. Gletsch. Glazialgeol.* **1985**, *21*, 403–407.

50. Paul, F.; Kaab, A.; Maisch, M.; Kellenberger, T.; Haeberli, W. Rapid disintegration of Alpine glaciers observed with satellite data. *Geophys. Res. Lett.* **2004**, *31*. [CrossRef]

51. Paul, F.; Machguth, H.; Kääb, A. On the impact of glacier albedo under conditions of extreme glacier melt: The summer of 2003 in the Alps. *EARSeL eProc.* **2005**, *4*, 139–149.

52. De Bono, A.; Peduzzi, P.; Kluser, S.; Giuliani, G. Impacts of Summer 2003 Heat Wave in Europe. Available online: http://www.unisdr.org/files/1145_ewheatwave.en.pdf (accessed on 14 October 2015).

53. Avian, M.; Kellerer-Pirklbauer, A.; Proske, H.; Wack, R.; Bauer, A. Assessment of Landscape Changes using High Resolution LiDAR data: The Proglacial Area of Pasterze Glacier and the DGSD of Zintlwald as Recent Examples in the Eastern Alps. Available online: https://www.researchgate.net/profile/Michael_Avian/publication/228954263_Assessment_of_Landscape_Changes_using_High_Resolution_LiDAR_data_The_Proglacial_Area_of_Pasterze_Glacier_and_the_DGSD_of_Zintlwald_as_Recent_/links/09e415114f5c646a66000000.pdf (accessed on 14 October 2015).

54. Andreassen, L.; Paul, F.; Kääb, A.; Hausberg, J. Landsat-derived glacier inventory for Jotunheimen, Norway, and deduced glacier changes since the 1930s. *Cryosphere* **2008**, *2*, 131–145. [CrossRef]

55. Bolch, T.; Kamp, U. Glacier mapping in high mountains using DEMs, Landsat and ASTER data. *Grazer Schr. Geogr. Raumforsch.* **2006**, *41*, 37–48.

56. Paul, F.; Bolch, T.; Kaab, A.; Nagler, T.; Nuth, C.; Scharrer, K.; Shepherd, A.; Strozzi, T.; Ticconi, F.; Bhambri, R.; *et al*. The glaciers climate change initiative: Methods for creating glacier area, elevation change and velocity products. *Remote Sens. Environ.* **2015**, *162*, 408–426. [CrossRef]

57. Paul, F.; Barrand, N.E.; Baumann, S.; Berthier, E.; Bolch, T.; Casey, K.; Frey, H.; Joshi, S.P.; Konovalov, V.; Bris, R.L.; *et al*. On the accuracy of glacier outlines derived from remote-sensing data. *Ann. Glaciol.* **2013**, *54*, 171–182. [CrossRef]

58. Pelto, M. Utility of late summer transient snowline migration rate on Taku Glacier, Alaska. *Cryosphere* **2011**, *5*, 1127–1133. [CrossRef]

59. Klein, A.G.; Isacks, B.L. Spectral mixture analysis of Landsat thematic mapper images applied to the detection of the transient snowline on tropical Andean glaciers. *Glob. Planet Chang.* **1999**, *22*, 139–154. [CrossRef]

60. Evans, I.S. Local aspect asymmetry of mountain glaciation: A global survey of consistency of favoured directions for glacier numbers and altitudes. *Geomorphology* **2006**, *73*, 166–184. [CrossRef]

61. Chinn, T. Glacier fluctuations in the Southern Alps of New Zealand determined from snowline elevations. *Arct. Alp. Res.* **1995**, 187–198. [CrossRef]

62. Rabatel, A.; Dedieu, J.-P.; Thibert, E.; Letréguilly, A.; Vincent, C. 25 years (1981–2005) of equilibrium-line altitude and mass-balance reconstruction on Glacier Blanc, French Alps, using remote-sensing methods and meteorological data. *J. Glaciol.* **2008**, *54*, 307–314. [CrossRef]

63. Bhardwaj, A.; Joshi, P.K.; Snehmani; Singh, M.K.; Sam, L.; Gupta, R.D. Mapping debris-covered glaciers and identifying factors affecting the accuracy. *Cold Reg. Sci. Technol.* **2014**, *106–107*, 161–174. [CrossRef]

64. Alifu, H.; Tateishi, R.; Johnson, B. A new band ratio technique for mapping debris-covered glaciers using Landsat imagery and a digital elevation model. *Int. J. Remote Sens.* **2015**, *36*, 2063–2075. [CrossRef]

65. Quincey, D.J.; Luckman, A.; Benn, D. Quantification of Everest region glacier velocities between 1992 and 2002, using satellite radar interferometry and feature tracking. *J. Glaciol.* **2009**, *55*, 596–606. [CrossRef]

66. Scherler, D.; Bookhagen, B.; Strecker, M.R. Spatially variable response of Himalayan glaciers to climate change affected by debris cover. *Nat. Geosci.* **2011**, *4*, 156–159. [CrossRef]

67. Smith, T.; Bookhagen, B.; Cannon, F. Improving semi-automated glacier mapping with a multi-method approach: Applications in central Asia. *Cryosphere* **2015**, *9*, 1747–1759. [CrossRef]

68. Shukla, A.; Arora, M.K.; Gupta, R.P. Synergistic approach for mapping debris-covered glaciers using optical-thermal remote sensing data with inputs from geomorphometric parameters. *Remote Sens. Environ.* **2010**, *114*, 1378–1387. [CrossRef]

69. Malenovský, Z.; Rott, H.; Cihlar, J.; Schaepman, M.E.; García-Santos, G.; Fernandes, R.; Berger, M. Sentinels for science: Potential of Sentinel-1, -2, and -3 missions for scientific observations of ocean, cryosphere, and land. *Remote Sens. Environ.* **2012**, *120*, 91–101. [CrossRef]

70. Martone, M.; Bräutigam, B.; Rizzoli, P.; Gonzalez, C.; Bachmann, M.; Krieger, G. Coherence evaluation of TanDEM-X interferometric data. *ISPRS J. Photogramm. Remote Sens.* **2012**, *73*, 21–29. [CrossRef]

71. Hölbling, D.; Friedl, B.; Eisank, C.; Tsai, T.-T. An object-based method for mapping landslides on various optical satellite imagery-transferability and applicability across spatial resolutions. In Proceedings of the RSPSoc Annual Conference, Aberystwyth, UK, 2–5 September 2014; pp. 2–5.

72. Torres-Sánchez, J.; López-Granados, F.; Peña, J.M. An automatic object-based method for optimal thresholding in UAV images: Application for vegetation detection in herbaceous crops. *Comput. Electron. Agric.* **2015**, *114*, 43–52. [CrossRef]